International Journal of Industrial Ergonomics 107 (2025) 103738

Contents lists available at ScienceDirect

International Journal of Industrial Ergonomics

journal homepage: www.elsevier.com/locate/ergon

Development of a parametric model of adult human ear geometry

Matthew P. Reed, Tyler R. Vallier *, Anne C. Bonifas

University of Michigan Transportation Research Institute, USA

ARTICLE INFO

Keywords:
Parametric ear model
Ear device design
CT scan ear geometry

ABSTRACT

Quantitative knowledge regarding the size and shape of the human ear is valuable for the design of hearing protection and audio devices. In this study, a retrospective analysis of computed tomography (CT) scans from a patient database was conducted in order to address the need for a three-dimensional parametric model of adult ear geometry. A template polygonal mesh was fit to extracted geometry of the pinna, canal, and adjacent scalp for 331 ears from 224 men and women aged 18–81 years. Principal component analysis demonstrated a large amount of variance in the position and orientation of the ears with respect to the skull. A regression analysis confirmed previous findings of sex differences in the increase of ear size with increasing age and demonstrated an effect of body mass index on ear position and orientation that has not been previously described.

1. Introduction

The size and shape of the human ear has been studied extensively (Farkas, 1978; Alexander et al., 2011; Fu and Luximon, 2020). The ear exhibits complex, visible geometry that varies enough across individuals that it has been proposed as a biometric identifier (Cintas et al., 2017; Kamboj et al., 2020). The size, shape, and location of the ear are critical inputs to the design of hearing protection and both in-ear and head-worn audio devices, including headphones, earbuds, and hearing aids (Liu, 2008; Ji et al., 2018; Lu et al., 2021). The size and shape of the ear affects the head-related transfer function (HRTF), which influences the ability of the listener to localize sound (Pollack et al., 2020).

Due to the variability of individual ears, hearing protection and hearing aids are often designed from molds made of the user's ear. Molding material is pressed into the canal and adjacent concha areas to capture the shape, then carefully removed and scanned to produce custom in-ear devices. Experienced audiologists are able to use the measured geometry to produce comfortable and effective devices that remain in place. Statistical modeling of ear molds has been conducted to characterize the distribution of ear shape in this important area (Paulsen et al., 2002; Baloch et al., 2011).

Despite the importance of ear shape for design applications, most prior studies of the whole pinna have reported linear dimensions between landmarks (Farkas, 1978; Niemitz et al., 2007; Sforza et al., 2009; Alexander et al., 2011). Although this information is useful for comparing ear dimensions across populations, it is difficult to apply to the design of three-dimensional (3D) products. In recent years, improvements in measurement and analysis methods have enabled 3D modeling of a large range of complex body structures, from faces to fingers and toes. However, few papers describe detailed 3D models of the ear. Several studies have used morphable template models to fit the geometry of the pinna (Chu et al., 2019; Fantini et al., 2021) but these studies have not included the adjacent scalp and canal.

Two recent studies have integrated 3D surface scans of the ear with scans of molds taken of the concha and outer canal. Lee et al. (2018) reported a large number of linear dimensions based on manual digitization of scan data from 230 Koreans and 96 Caucasians. Fan et al. (2021a, 2021b) obtained surface scans and canal molds from the left and right ears of 700 Chinese adults. Summary statistics on dimensions of the pinna and outer canal were reported. However, neither of these recent studies reported the generation of an integrated statistical model of ear shape.

This paper describes the development of a parametric model of the adult human ear based on geometry extracted from computed tomography (CT) scans taken as part of medical care. CT scanners obtain detailed images of structures in the body by rotating an x-ray head and detector around the patient's body. The geometry of anatomical components can be extracted from these images by specifying a range of density (attenuation) corresponding to the desired tissue (for example, skin or bone). CT scans have been used in prior research relating to the middle and inner ear (Fernanda et al., 2014; Balouch et al., 2023), but do not appear to have been used to create integrated statistical models of the pinna and canal. For the current study, CT scans were obtained retrospectively from a patient database and de-identified under

* Corresponding author.
E-mail addresses: tylerval@umich.edu, tylervallier8@gmail.com (T.R. Vallier).

https://doi.org/10.1016/j.ergon.2025.103738
Received 10 April 2024; Received in revised form 13 January 2025; Accepted 30 March 2025
Available online 9 April 2025
0169-8141/

approval of an Institutional Review Board.

Skin surface data that included the detailed ear geometry from the scalp and pinna through the canal to the middle ear were extracted along with the skull from a convenience sample of scans from 224 men and women ages 18–81 years. A total of 331 ears were extracted after aligning each head to a common coordinate system. The number of ears extracted was smaller than twice the number of subjects due to distortions of one ear for some subjects due to the supports used to position the patients head during the scan. Using custom software and a semi-automated technique, a polygonal template with 60k vertices was fit to each ear. Principal component analysis (PCA) and regression were used to explore the primary modes of size and shape variance along with the associations with covariates such as sex, age and BMI. The resulting dataset and model have broad applicability to ear-related design problems.

2. Methods

2.1. Subjects and CT scans

De-identified CT studies were obtained from the radiology archives at the University of Michigan Medical Center using protocols approved by a U-M Institutional Review Board (HUM00004842). The patient age, sex, stature (erect standing height), and body weight were obtained for each study. Data were gathered from scanning protocols with the patient prone (face down) or supine (face up). Due to the action of gravity on the tissues, the data from these poses are slightly different, so these effects were assessed statistically. The resolution of the CT images was 0.625 mm between slices and in-plane resolution of 0.7–1 mm for the prone studies and 0.3–0.5 mm for the supine studies. Table 1 shows summary statistics for the covariates of the 224 subjects. An effort was made to obtain approximately equal numbers of male and female subjects well distributed across the adult age range, but otherwise this is a convenience sample. Nonetheless, Table 1 shows that the distribution of stature, body mass index, and age is large and spans a large proportion of the U.S. population. Two ears were obtained from 107 subjects while the remaining subjects contributed a single ear, due to problems with the contralateral ear such as deformation of the pinna due to head supports used during scanning. A total of 155 ears were obtained from prone scans and 176 from supine (see Table 2).

2.2. Extracting skull and skin surfaces

After verifying that the ears did not exhibit any anomalies, such as modifications beyond typical piercings or overt pathological changes, the geometry of the skin of the head was extracted using semi-automated methods in Mimics software (https://www.materialise.com/). The skin surface was extracted using a window of −325 to 200 HU Hounsfield units (HU), which was manually adjusted as needed to obtain a clean representation of the skin surface. The surfaces of the sinuses and other areas within the head that were not of interest were manually removed. The skull was extracted using a standard bone thresholding window of 226–3071 HU.

Table 1A
Male Age and Body Dimensions: 160 ears; 83 Right, 77 Left. Values in parentheses are comparable numbers for U.S. adults (Fryar et al., 2021).

Male	Min	5th %ile	Median	95th %ile	Max
Stature (mm)	1658	1625 (1628)	1778 (1754)	1896 (1874)	1981
BMI (kg/m^2)	19.1	20.7 (20.8)	26 0.6 (28.5)	34.0 (41)	42.2
Age (yr)	18.0	21.3	43.0	69.0	81

Table 1B
Female Age and Body Dimensions: 171 ears; 79 Right, 92 Left. Values in parentheses are comparable numbers for U.S. adults (Fryar et al., 2021).

Female	Min	5th %ile	Median	95th %ile	Max
Stature (mm)	1461	1524 (1498)	1626 (1613)	1750 (1725)	1854
BMI (kg/m^2)	14.8	19.4 (19.7)	26.0 (28.4)	41.1 (44.6)	48.0
Age (yr)	19.0	20.8	42.0	72.5	79

Table 2
Fitting statistics between the fitted template and the target.

Statistic[a]	Value
Median of median fit discrepancies[b]	0.03 mm
Median of 99.9th percentile of fit discrepancies	0.44 mm

[a] Computed across all ears in the dataset.
[b] Computed point-to-point; point-to-polygon values would generally be smaller.

2.3. Aligning and extracting ears

The locations of the left and right porion and infraorbitale landmarks, which together define the Frankfurt plane, were digitized on each skull (Fig. 1). The porion lies at the superior margin of the external auditory meatus in the temporal bone, and the infraorbitale landmark is the lowest point on the inferior margin of the orbit. All of the skull landmarks were digitized by the same person. Landmarks were digitized three times on a randomly selected set of 10 skulls to quantify repeatability. The median (across subjects) of the median landmark discrepancy was 0.40 mm. That is, half of the measured landmark locations were less than 0.4 mm from the mean value obtained from three measurements. The median (across subjects) 95th percentile landmark discrepancy was 0.83 mm. The root-mean-square (RMS) discrepancy across all ears and landmarks was 0.89 mm, and the 95th percentile RMS value was 1.7 mm.

The head was aligned to a right-handed coordinate system with the origin located at the midpoint between the porion landmarks, the Y axis passing through both porion landmarks and positive to the left, X axis positive forward, and the Z axis positive upward. Thus, the ear geometry

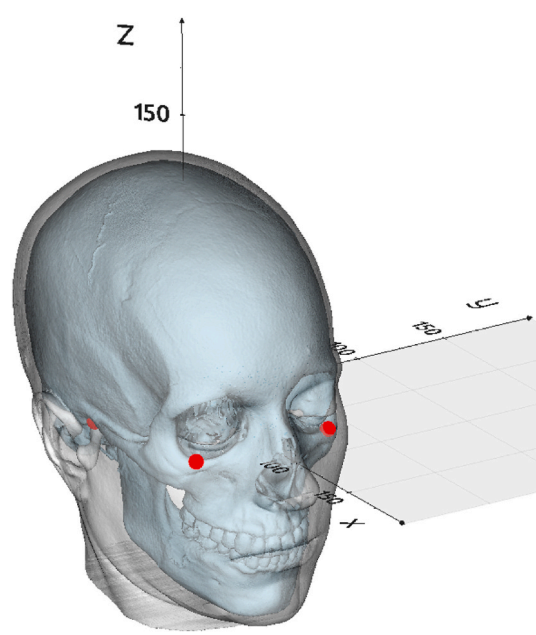

Fig. 1. Head-centered coordinate system based on porion and infraorbitale landmarks (red spheres). (For interpretation of the references to color in this figure legend, the reader is referred to the Web version of this article.)

analysis was conducted in a head-centered coordinate system, rather than local to the ear. The left ears were mirrored to the right side around the XZ plane to facilitate analysis.

The ear area including the adjacent scalp was automatically extracted after head alignment (Fig. 2). The middle ear geometry was then manually removed at the estimated location of the tympanic membrane (ear drum) using a manual procedure. In the supine scans with 0.625-mm resolution, the ossicles (middle ear bones) could be visualized on some of the scans, enabling the ear drum location to be estimated within about 1 mm. Based on review of several dozen scans, the typical location of the ear drum with respect to the exterior geometry of the middle ear was determined. This information was then used in a manual process to remove the middle ear geometry and cap the canal at the estimated ear drum location.

2.4. Manual landmark digitization

To aid in analysis of the ear geometry, a set of landmarks were manually located on each ear. Fig. 4 shows the landmarks. The landmarks were chosen to facilitate template fitting and to maximize homology in certain areas, rather than to match landmarks used in prior studies. For example, points on the helix were matched with points on the back of the pinna to facilitate template fitting. All of the landmarks were digitized by the same person. Landmarks were digitized three times on a randomly selected set of 10 ears to quantify repeatability. Landmarking discrepancies were expressed as the 3D distance of the measured landmark location from the mean for that landmark on that ear. The median (across ears) of the median landmark discrepancy was 0.34 mm. That is, half of the measured landmark locations were less than 0.4 mm from the mean value obtained from three measurements. The median (across ears) 95th percentile landmark discrepancy was 1.2 mm. The root-mean-square (RMS) discrepancy across all ears and landmarks was 0.73 mm, and the 95th percentile RMS value was 1.9 mm. Relative to the mean pinna height of 56 mm, these values represent 1.2 % and 3.3 %, respectively.

2.5. Fitting homologous mesh

To enable statistical shape analysis, a polygonal template mesh was fit to each ear. The template was generated by a bootstrapping procedure that involved fitting a subset of data, computing the mean, then refitting the data with the mean ear geometry. Experimentation with tradeoffs between mesh resolution, fitting time, and fitting quality led to the selection of a template mesh with 60040 vertices and 119655 triangles.

The template mesh was fitted to the ear geometry in a multistep process using openly available libraries as well as custom software written in Python for this application making extensive use of the *vedo* wrapper for the *vtk* library (Musy et al., 2023; Schroeder et al., 2006). First, the extracted ear geometry was smoothed by using the Poisson reconstruction filter from the *pymeshlab* library (Muntoni and Cignoni 2021) with the *pointweight* parameter set to 4. Reconstructing the surface improved the consistency of normals and addressed a problem in which vertices from both sides of the skin were interposed, resulting in a jagged surface. The reconstructed mesh typically had 120k vertices and 240k polygons. The median across ears of the median distances between the

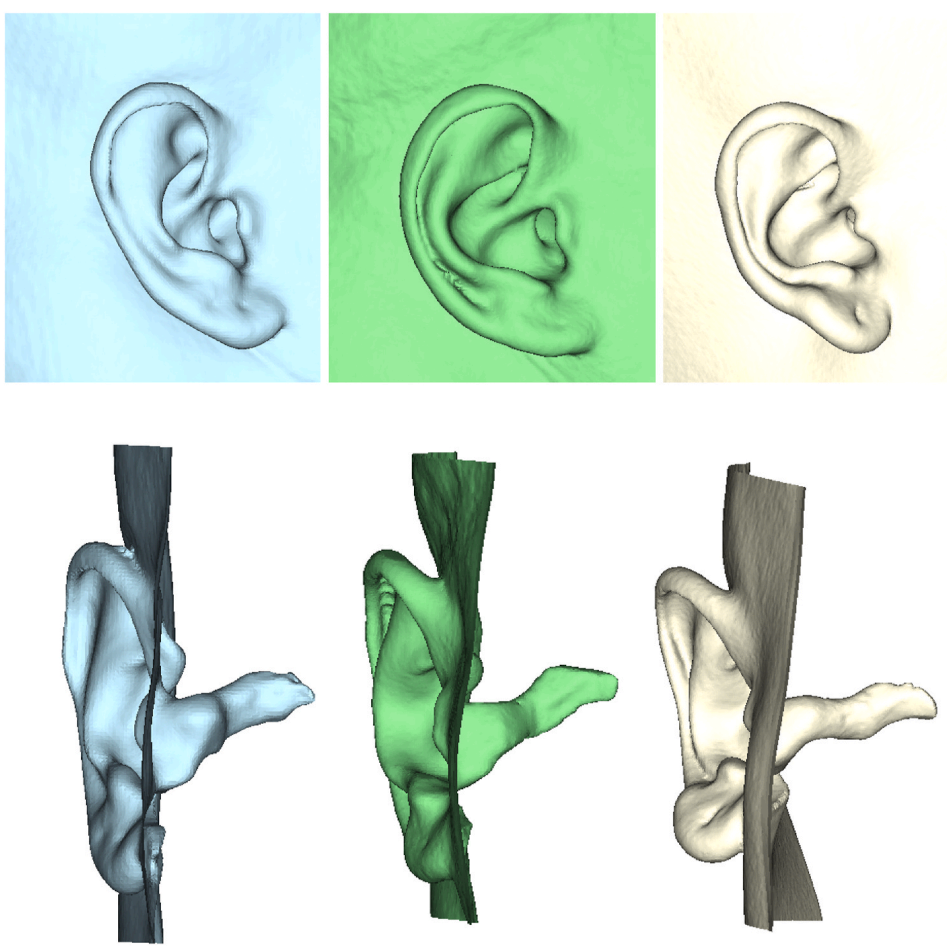

Fig. 2. Example ears extracted from CT in lateral view (top) and front view (bottom). The canals are truncated at the estimated ear drum (tympanic membrane) location.

original and reconstructed meshes was 0.008 mm; the 95th percentile median was 0.018 mm. The median 99.9th percentile distance was 0.18 mm.

In addition to the manually digitized landmarks, a set of landmarks were automatedly generated in the canal and on the perimeter of the scalp section (Fig. 3). The goal of the canal landmarking procedure was to ensure a high level of homology in the canal fitting, despite the canal lacking well-defined landmarks. Using custom software, a process similar to the median axis transform was used to place points along the approximate centerline of the canal, starting just medial to the ear drum. The algorithm generated the largest sphere that would fit within the canal at the current Y-axis (medial-lateral) location, then stepped outward repeating the process out to the Y plane of the tragion landmark. A cubic interpolating spline was constructed connecting the centers of the spheres, and this spline was sampled at 15 evenly spaced points to obtain the canal landmark set. In addition, perimeter points were generated in two rows along all four edges of the scalp boundary to anchor that area during the morphing process.

An initial non-rigid landmark-to-landmark morph was performed using a radial-basis-function (RBF) interpolator. The algorithm was implemented with the RBFinterpolator function in the Python language *scipy* library (Peterson et al., 2020) using a multiquadric kernel with parameter values $epsilon = 0.1$ and $smoothing = 0.001$. This initial step matched the landmarks of the template to the corresponding locations on the target ear within 0.01 mm while smoothly morphing the geometry between the landmarks.

After manual landmarking, the fine fitting of the template to the target was accomplished fully automatically using an iterative algorithm implemented in Python. At each iteration, a set of 8000 vertices were randomly selected on the template along with the 2000 vertices currently having the largest distance from the target. For each of the source vertices, a "close" vertex on the target was sought, subject to weighting and distance filtering criteria. Specifically, the search radius was limited to 3 mm and the discrepancy in the direction of the normal at the source and target points was penalized, so that points with similar normal were favored. Specifically, a normal error of 15° was considered to be equivalent to a distance of 3 mm. These error penalties were combined linearly. Hence, if the closest point is less than 3 mm, a larger normal error was accepted, except that in no case could the normal error exceed 45°. This prevents the algorithm from mistakenly matching a point on the opposite side of the thickness of the pinna.

A multiquadric RBF morph was performed using the manually and automatically defined landmarks used in the first step, as well as the ~10k template vertices for which target points were identified. The

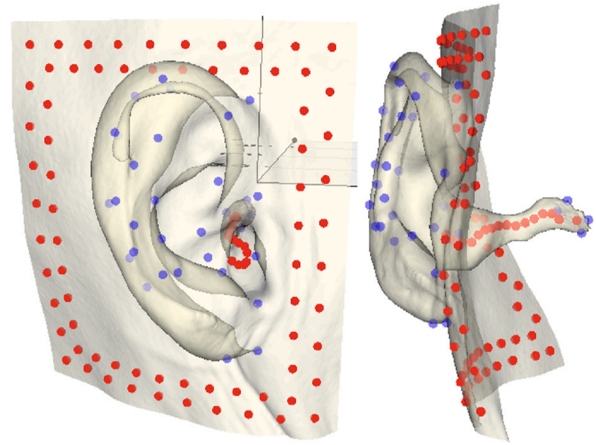

Fig. 4. Manual (blue) and automatically generated (red) landmarks. (For interpretation of the references to color in this figure legend, the reader is referred to the Web version of this article.)

epsilon (scaling) value was 0.5 and the smoothing parameter was 0.01 mm. The scaling parameter controls the range of points that are influential around a particular point, and the smoothing parameter forces the interpolator to fit the specified points within this criterion. Overall, this "normal aware" fine fitting enabled the thin areas of the pinna to be fit accurately and helped to maximize homology along the areas of high curvature on the helix and antihelix. After some experimentation, four iterations of this process were applied to each ear.

The distances between the fitted template and the target at each template vertex were computed to assess the goodness of fit. The median of the median fit discrepancies (point-to-point) across ears was 0.03 mm, with a median 99.9th-percentile value of 0.44 mm, which is less than the original CT scan resolution. Most of the fit discrepancies larger than 0.5 mm were in the area of the ear lobe and none was in the concha or canal areas.

2.6. Statistical analysis

A principal component analysis was conducted on the coordinates of the fitted template vertices. The coordinates for each ear were flattened into a single vector, concatenated row-wise with the data from the other ears, and a singular value decomposition was computed on this matrix using *scipy.linalg.svd* (Peterson et al., 2020). The 331 resulting

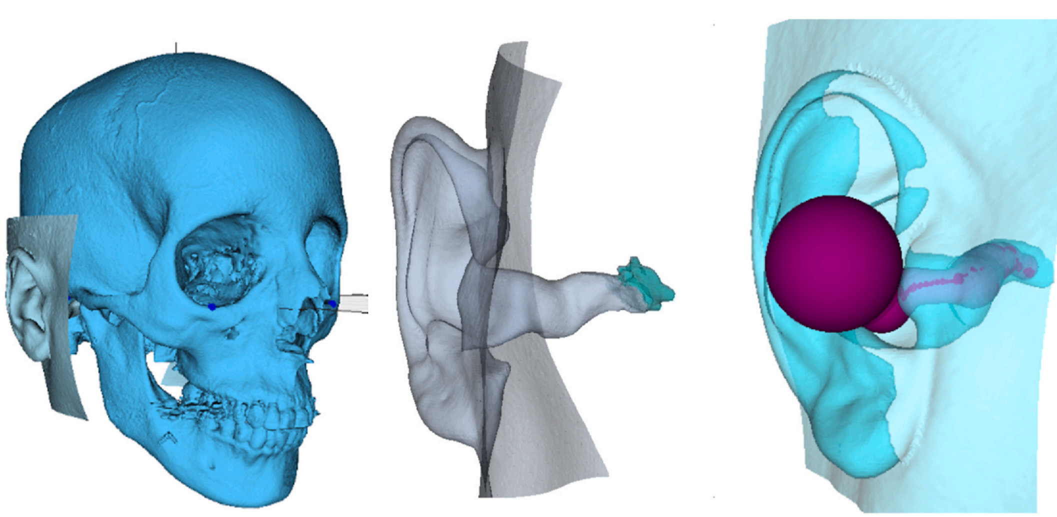

Fig. 3. Illustration of steps in the data processing pipeline: (a) extracting the ear geometry in skull coordinates, (b) removing the middle ear at the estimated eardrum location, and (c) estimating the centerline of the canal by sphere fitting and splining.

eigenvalues and eigenvectors were retained for analysis. To quantify the effects of condition variables and covariates, linear regression analyses were conducted predicting principal component scores from variables including sex, stature, body mass index, ear side (left/right), and patient posture (prone/supine). The predicted scores were used to reconstruct ear geometry.

3. Results

3.1. Mean ear

Fig. 5 shows the mean ear from several angles. The high level of homology is evident in the crispness of the features on the helix and antihelix, and the first and second bend of the canal are readily evident.

3.2. Visualizing principal components

Fig. 6 illustrates the first 8 principal components using ears generated by manipulating each PC by ±3 standard deviations (SD) while holding the others at zero (the mean). The primary modes of variance are related to the position and orientation of the ear with respect to the skull (i.e., with respect to the coordinate system). The first PC is strongly related to the lateral position of the ear and hence to head breadth. A relatively clear relationship with local ear size is not seen until PC4. In interpreting Fig. 5, consider that the PCA is partitioning variance in the vertex coordinates, and a large number of vertices are on the scalp portion of the model (approximately 25000 in the scalp, 28000 in the pinna, and 7000 in the canal beyond the first bend). Hence the lateral position of the ear (including the scalp) represents a large amount of variance across this sample with widely varying head size, allowing PC1 to account for nearly half of the total. Fig. 5 shows that the first 8 PCs account for about 91 % of the variance in the model; 14 PCs are necessary to reach 95 % of variance. Note, however, that considerable variation of interest for a particular design problem could be associated with higher PCs.

3.3. Effects of covariates

The relationship between ear size, shape, and position in relation to covariates was examined using linear regression predicting PC scores. All PCs were retained for this analysis, so the results are mathematically equivalent to predicting vertex coordinates directly.

Fig. 7 compares the mean prone and supine ears. The supine ear lies slightly rearward of the prone ear, relative to the skull, consistent with the effects of gravity on the ear and adjacent soft tissue. In the analysis below, this effect is neglected, because approximately equal numbers of prone and supine ears were analyzed.

Fig. 8 shows the mean male and female ears, without adjusting for any other covariates. As expected, the ears have visually similar shape, but the female ear is smaller and angled out slightly more at the top. Fig. 9 shows the effects of age for male and female ears, demonstrating a large effect of age on ear size and a small effect on fore-aft position. The male effect of age on size is slightly larger, and the ears shift rearward more with age for men than for women.

The effect of stature and BMI within sex are shown in Fig. 10. Stature was varied from the 5th percentile to 95th percentile values for the US population (1627–1870 mm for men and 1500–1750 mm for women) and BMI was varied using the same values for both sexes (22–40 kg/m^2). Stature, a surrogate for overall body size, has a similar effect for both men and women. BMI has a surprisingly large association with the lateral position and angle of the lower portion of the ear, consistent with the ear canal being stretched over time as the soft tissue accumulates in the area. The effects are similar for men and women.

3.4. PCA on the pinna (auricle)

For some applications, an analysis local to the pinna may be more useful than preceding analysis in head coordinates. Fig. 11 shows the results of PCA on points in the pinna and the outer area of the canal. The analysis was conducted after translating the tragion location on each ear to the origin.

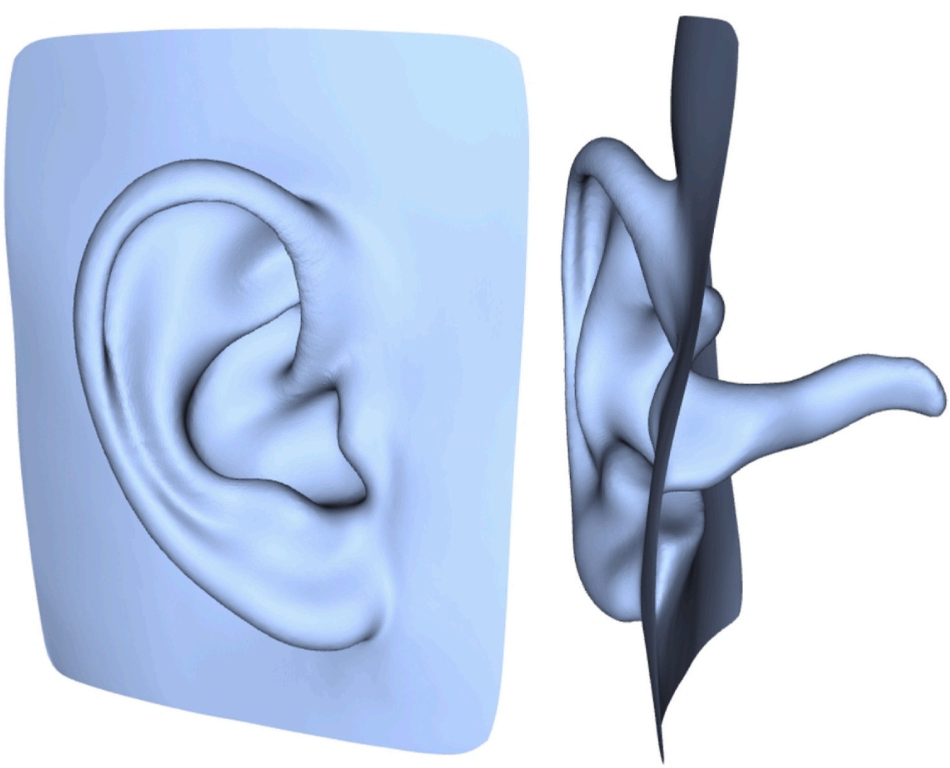

Fig. 5. a. Multiple views of the mean ear (N = 331) with flat shading to show the polygon resolution.

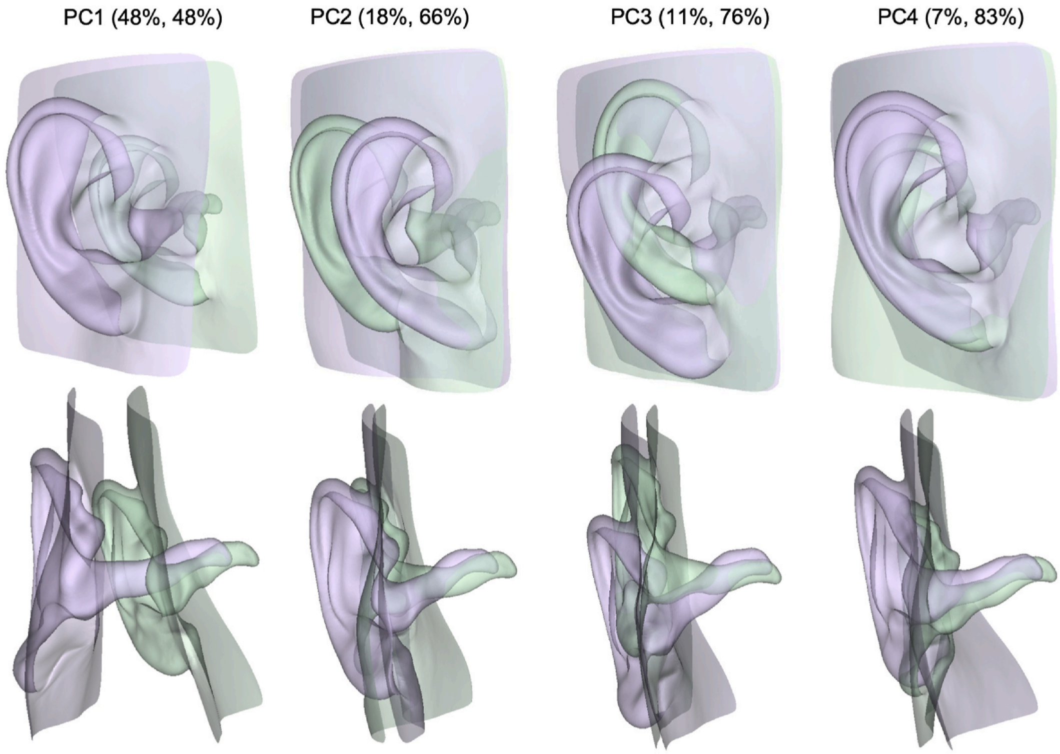

Fig. 6A. Illustrations of the first 4 modes of variance (principal components) obtained by varying each PC by ±3 standard deviations while holding the others at zero (i.e., the mean). The numbers above each figure are the percentage of variance accounted for by the PC and the cumulative variance including that PC and all lower numbered PCs. The colors are arbitrary, representing the extremes of each component. Note that the sign of each component is also arbitrary. (For interpretation of the references to color in this figure legend, the reader is referred to the Web version of this article.)

In this case, the first PC is strongly related to the overall size of the pinna, while the second is related to the front-view angle. The ear rotation in sagittal view is associated with PC4.

3.5. Effects of covariates on the pinna

Fig. 12 through 14 show the association between covariates and the size and shape of the pinna. The male and female ears appear much more similar when the effect of head breadth is removed (compare with Fig. 9). The effect of age is similar between the whole-ear and pinna models, as age primarily affects the dimensions of the pinna. The effects of stature and BMI in the pinnal model are also similar to the whole-ear model.

3.6. Generative modeling for design

For design evaluations, investigating the fit relative to all of the ears in the database may not be practical. Consequently, it may be valuable for some applications to have a smaller number of ears that represent a wide range of certain relevant characteristics. A boundary model approach in PCA space was applied in two coordinate systems. First, ears were generated in the space of the first three principal components relative to the skull coordinate system. These ears are particularly relevant to the design of over-ear devices, such as headphones. Under the assumption that non-accommodation could occur due to a device being either too small or too large for a particular ear feature, ears were generated that span 95 % of the variance on the first three PCs. Referring to Fig. 11, the first three PCs account for 76 % of the total variance. Boundary ears were generated at the extremes of each axis on the 95 % multinormal enclosure ellipsoid (6 ears) and at the 8 intermediate points on the boundary for a total of 14 ears. Fig. 15 shows these boundary ears relative to the mean ear and individually. The generated ears span a wide range of size, locations, and orientations in the head-centered coordinate system.

Fig. 16 shows boundary ears computed in the same manner as those in Fig. 15 for the PCA conducted on the pinna geometry centered at the tragion. Compared with the ears generated using the whole-ear model, these boundary ears are more relevant for the design and assessment of in-ear devices. In these representations, the variability in size and shape of the pinna is more evident, including readily apparent variation in the shape of the concha and tragal notch.

4. Discussion

4.1. Summary and novelty

This paper has presented the development of a statistical model of adult ear geometry based on adapting prior methods to a novel data source. The dataset and statistical models presented here are novel in several important ways. This is the first reported statistical shape model of pinna and canal geometry based on CT data and incorporates a larger sample size than previously published 3D ear datasets based on homologous template fitting. CT data has not been used for prospective studies because of the ethical concerns regarding exposure to radiation, but the retrospective nature of the current study using medically necessitated scans eliminates that concern. The use of CT allows the full canal to be included in the same model as the pinna. The resolution and accuracy are greater than typical of external optical scanners, and the fitting methodology resulted in high accuracy and good homology across the ear.

The use of CT provides considerable advantages over the primary methods used in recent large-scale studies that combined hand-held optical scanning with ear molding. Less manual manipulation of the data is needed, because the entire geometry is extracted in one pass, and hence the alignment of the pinna and canal data is not a concern. The statistical model may also be useful for fitting sparse or noisy data

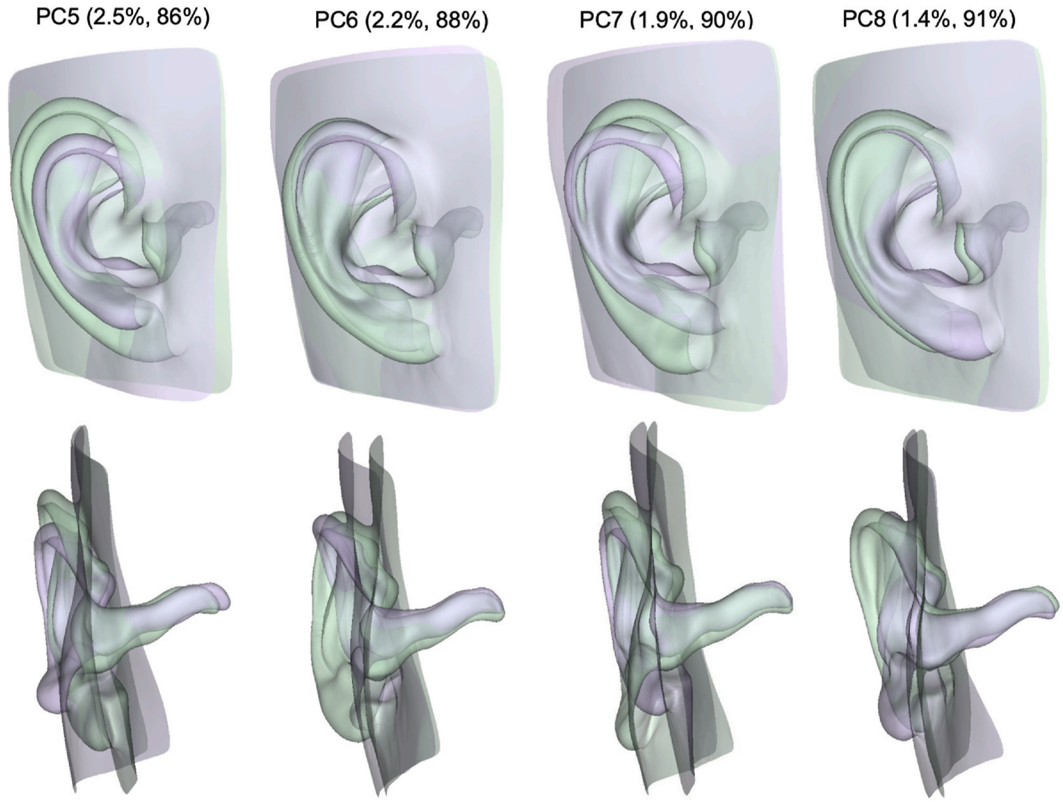

Fig. 6B. Illustrations of the 5th through 8th modes of variance (principal components) obtained by varying each PC by ±3 standard deviations while holding the others at zero (i.e., the mean). The numbers above each figure are the percentage of variance accounted for by the PC and the cumulative variance including that PC and all lower numbered PCs. The colors are arbitrary, representing the extremes of each component. Note that the sign of each component is also arbitrary. (For interpretation of the references to color in this figure legend, the reader is referred to the Web version of this article.)

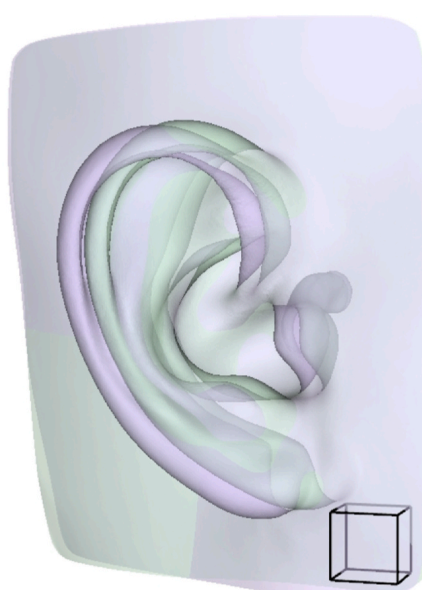

Fig. 7. Mean ears from prone (green) vs supine (purple) postures. All ears are represented in skull-based coordinates, so the difference in fore-aft position of approximately 4 mm represents the opposite effects of gravity on soft tissue movement relative to the skull in the two postures. Wireframe cube has 10-mm edge length and is aligned to the head coordinate system. (For interpretation of the references to color in this figure legend, the reader is referred to the Web version of this article.)

obtained from other measurement modalities such as optical scanners and for imputing canal geometry from the size, shape, and location of the pinna.

This is also the first large-scale ear geometry dataset gathered in head-centered coordinates, which revealed a large amount of new information about the variance in ear position and orientation, including the substantial amount of variance in canal size, shape, and orientation relative to the temporal bone. The ability to express the ear geometry relative to the skull with high accuracy is another advantage of the CT-based technique. This analysis is the first to describe quantitatively the substantial effects of BMI on ear placement and orientation, suggesting that the ear canal is lengthened in individuals with higher BMI.

Boundary ear models potentially useful for design were generated in two coordinate systems, demonstrating the flexibility of the dataset. Many other analyses of ear regions could be conducted. For example, an analysis could focus exclusively on the concha and outer canal area to develop design targets for earbuds or hearing aids. Note that a PCA conducted on a small area can be used to generate whole ears consistent with the local targets.

The value of the homologous template fitting is emphasized by the nature of other recent publications, which have tabulated large numbers of dimensions based on manually extracted landmarks. With the current statistical model, any point-to-point dimensions can be extracted programmatically, replicating the prior work. But the 3D statistical models have far more value for use in 3D fitting trials.

4.2. Limitations

The study has limitations that may affect the applicability of the data. The sample size is larger than most prior 3D studies, but a larger sample would be valuable because of the large amount of variability in

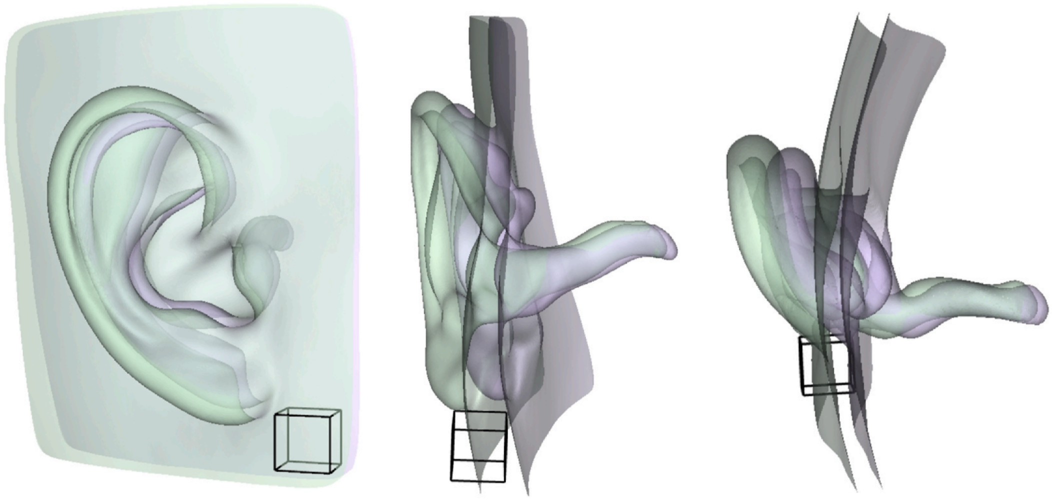

Fig. 8. Mean male (green) and female (purple) ears. Wireframe cube has 10-mm edge length and is aligned to the head coordinate system. (For interpretation of the references to color in this figure legend, the reader is referred to the Web version of this article.)

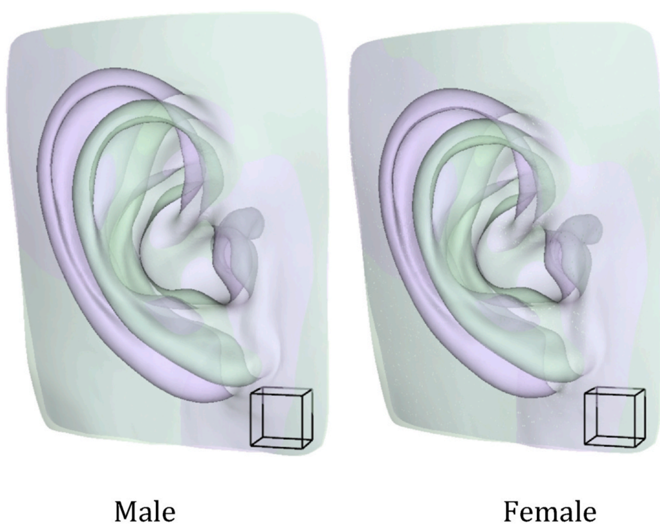

Fig. 9. Effect of age for male (left) and female (right). Older ears (purple) are larger. Wireframe cube has 10-mm edge length and is aligned to the head coordinate system. (For interpretation of the references to color in this figure legend, the reader is referred to the Web version of this article.)

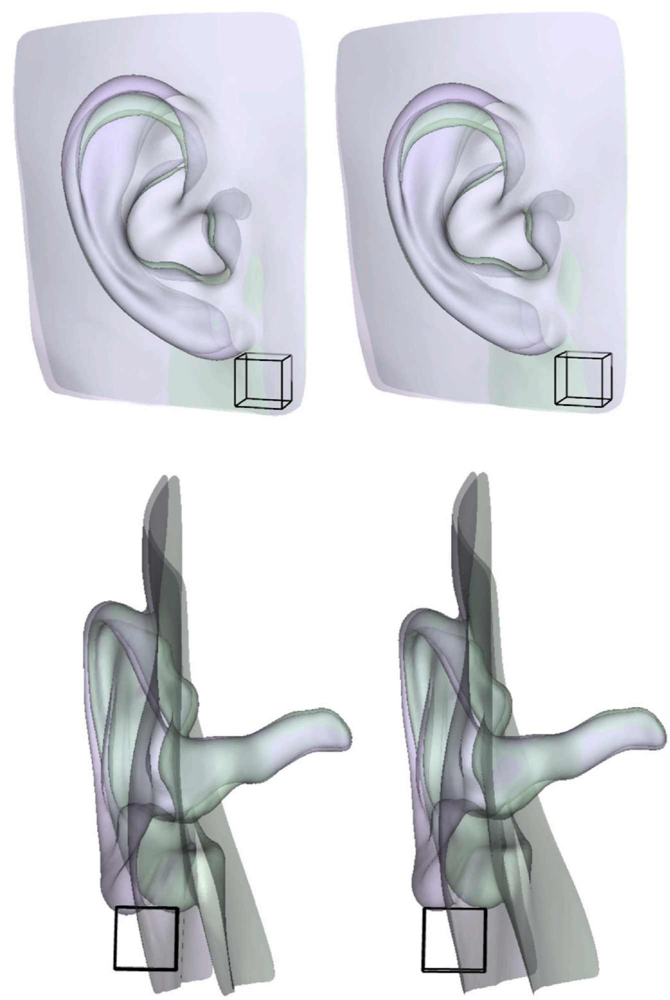

Fig. 10. Top: Illustrations of the effects of stature (5th to 95th percentile within sex, and bottom: BMI (22–40 kg/m^2); male left, female right.

ear shape. Although approximately equal numbers of male and female ears were analyzed, and a wide range of adult ages was represented, the distribution of geographical region of origin for the subjects is unknown. The population may not be representative of the U.S. population, which includes people with a wide range of regions of origin, although the large number of subjects obtained essentially at random from the radiology archives at a large U.S. teaching hospital suggests that the data will have broad utility.

The distribution of available covariates (stature and BMI) closely matches these ranges for the U.S. population. However, the sizes and shapes of ears from a different population could be different. Lee et al. (2018) showed small but systematic differences in linear dimensions between Korean and "Caucasian" populations. Utilizing these methods with CT studies from other populations would enable comparative studies. The statistical shape model developed in this work could also be used to fit 3D scan data from other studies, thereby putting all the data into the same shape space and enabling quantitative comparison of populations on dimensions of interest.

The eardrum location could not be readily visualized in most of the scans, although as noted the ossicles were visible in some scans, enabling the development of a manual method for estimating the eardrum location based on the shape of the transition from the canal to middle ear. Although we were not able to systematically quantify this error, we

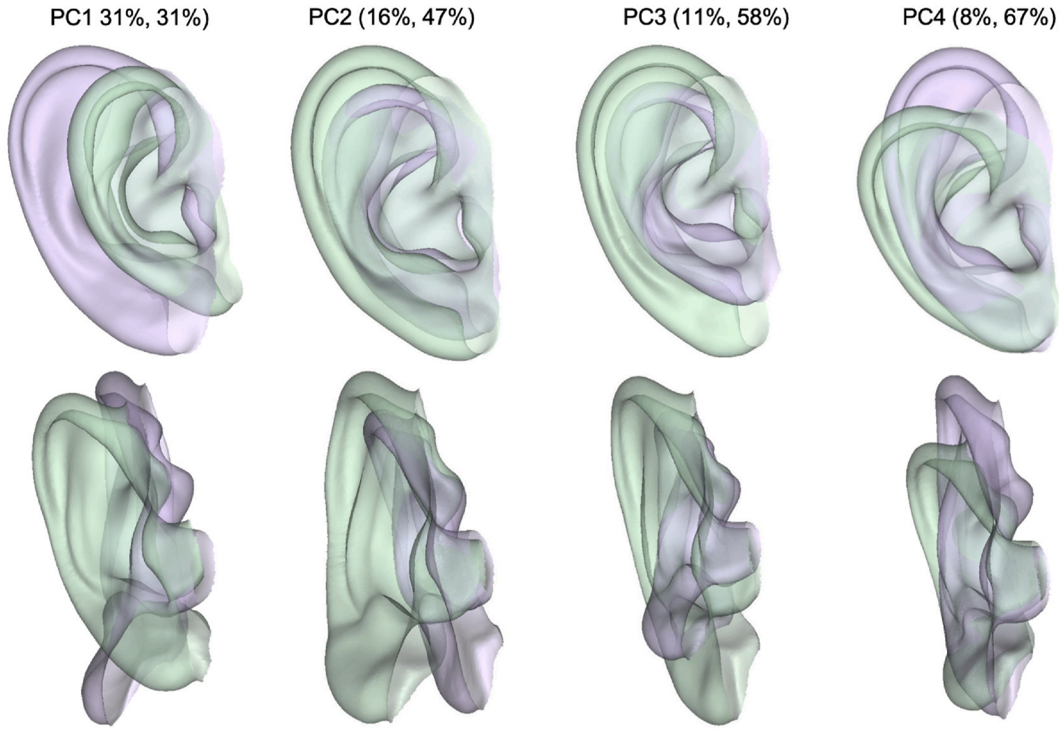

Fig. 11A. Illustrations of the first 4 modes of variance (principal components) **of the pinna** obtained by varying each PC by ±3 standard deviations while holding the others at zero (i.e., the mean). The numbers above each figure are the percentage of variance accounted for by the PC and the cumulative variance including that PC and all lower numbered PCs.

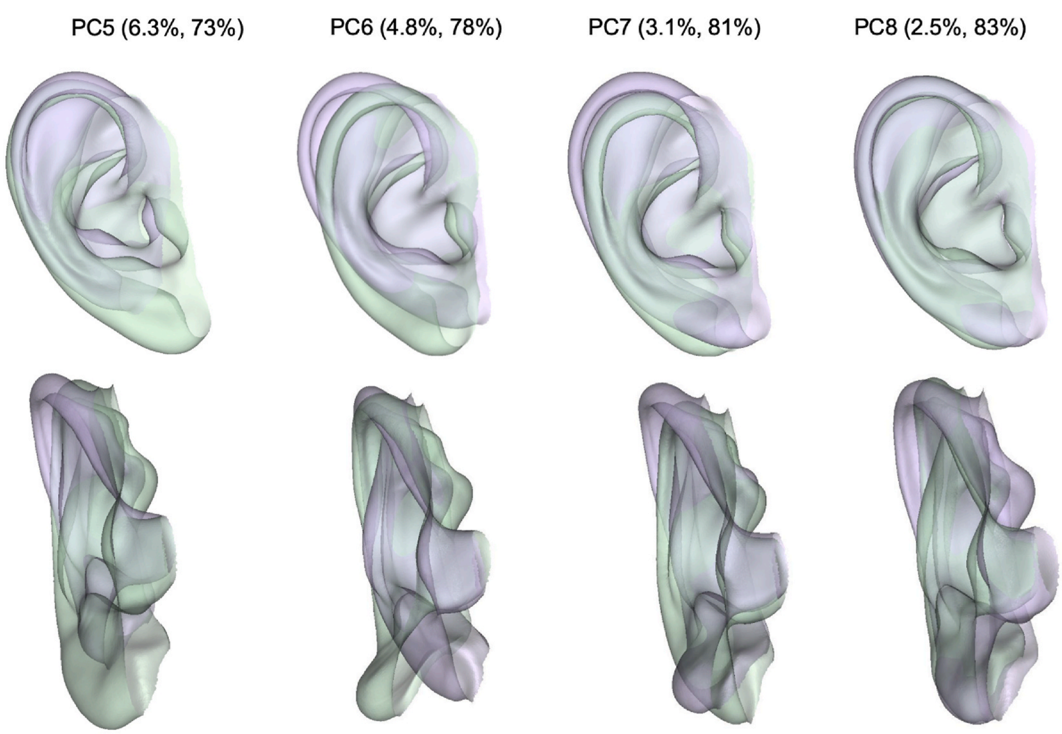

Fig. 11B. Illustrations of the 5th through 8th modes of variance (principal components) **of the pinna** obtained by varying each PC by ±3 standard deviations while holding the others at zero (i.e., the mean). The numbers above each figure are the percentage of variance accounted for by the PC and the cumulative variance including that PC and all lower numbered PCs.

estimate that the lateral position of the eardrum is typically within 2 mm of the manually identified location. We note that no prior large-scale ear geometry study has included any estimate of the eardrum location, so the current study represents a step forward, even with this uncertainty.

The supine and prone poses used in the patient scanning were shown to differ with respect to the ear location relative to the skull, but not with

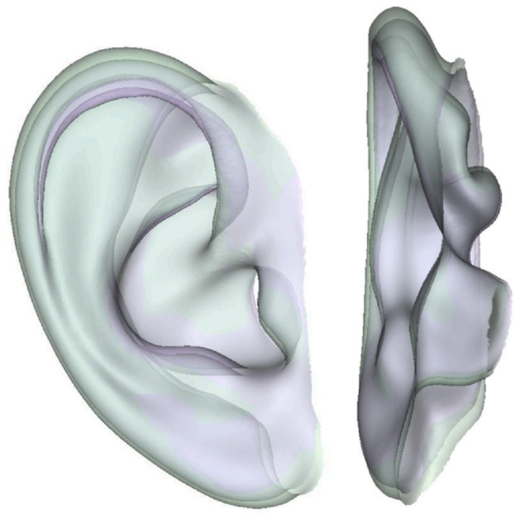

Fig. 12. Mean male (green) and female (purple) pinnae. (For interpretation of the references to color in this figure legend, the reader is referred to the Web version of this article.)

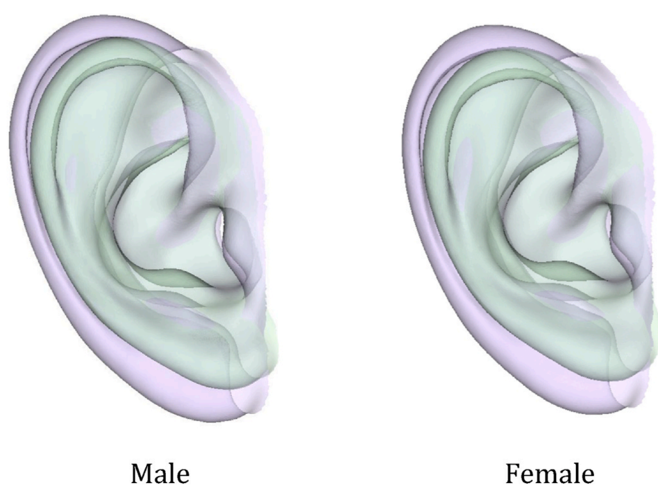

Fig. 13. Effect of age for male (left) and female (right). Older ears (purple) are larger. (For interpretation of the references to color in this figure legend, the reader is referred to the Web version of this article.)

respect to shape otherwise. Given the apparent and expected effects of gravity on the ear location, we can anticipate that the ears will be slightly lower relative to the head when the user is upright, and that the ears are likely to move relative to the head during dynamic activities or changes in posture. These are potential topics for future research. We can hypothesize that most of the change in ear position occurs due to changes in the outer canal, i.e., outside of the temporal bone, resulting in changes in the shape of the canal, but more research will be needed to quantify these effects.

The Poisson reconstruction used in the fitting process introduced a rounded inward end to the canal that is unrealistic; the base of this "bubble" is the estimated location of the ear drum. The ear location relative to the skull was slightly different in prone and supine poses, consistent with the action of gravity on the soft tissue. This effect was small compared with other aspects of variability and is effectively nulled out on the anterior-posterior axis by the use of approximately equal numbers of prone and supine scans. However, given the observed soft-tissue mobility, ear locations with the head upright may be slightly lower than those observed in these prone and supine scans. All of the scans used in this study were screened for pathology, injury, or other

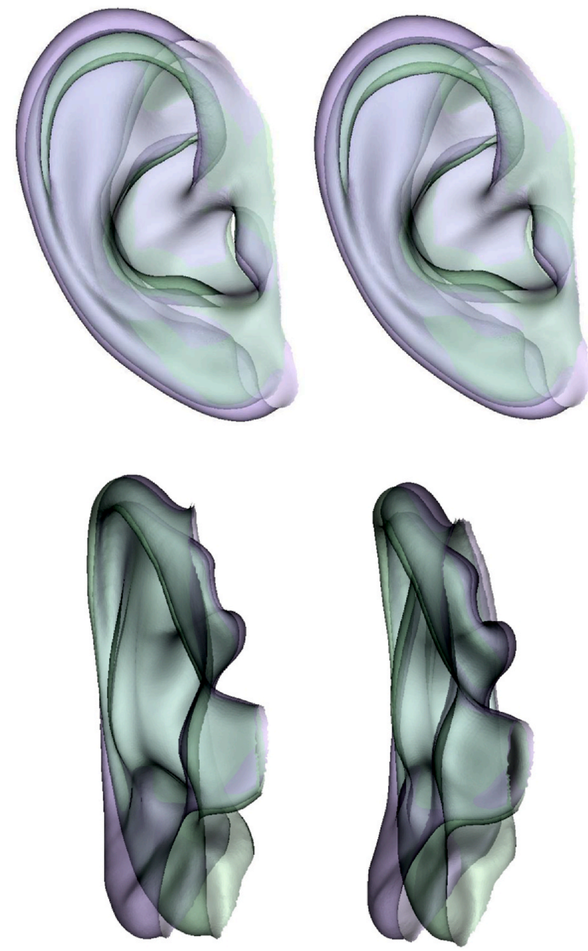

Fig. 14. Top: Illustrations of the effects of stature (5th to 95th percentile within sex, and bottom: BMI (22–40 kg/m^2); male left, female right.

factors that could affect the ear geometry. The ears used for this analysis were free of apparent pathology, but all individuals scanned were patients with a medically indicated need for a CT scan, and hence like any other patient population may not be fully representative of the general population. The extraction of the ear geometry involved thresholding the CT density to identify the skin boundary. As noted in the methods section, we selected a threshold window in the range of −325 to 200 HU to define the skin. Because the outer skin boundary occurs at a sharp density transition between air and skin, the outer boundary that we are modeling is less sensitive to the choice of threshold. The areas of the ear most affected by the threshold are in the region where the ear joins the scalp, where differences in the window HU values may have affected the outcome by a maximum of about 1 mm.

The PCA boundary ear presentation is intended as a demonstration of the major modes of variability in the dataset. These ear instances may not be appropriate or useful for any particular analysis. As with all such applications of the PCA method for boundary case generation, the choice of the number of PCs to retain, the enclosure percentage selection, and the number of boundary cases all influence the resulting family of shapes. Moreover, a PCA on vertex locations is strongly influenced by the choice of origin and the distribution of vertices in the geometry. This is clear in the results presented here, where a set of boundary ears generated after centering on the tragion landmark and limiting the analysis to the pinna produces substantially different geometry. We do not recommend making final design decisions using boundary cases; these are best used as aids in the initial phases of design, with virtual fit testing against the entire dataset used to produce quantitative estimates of population accommodation.

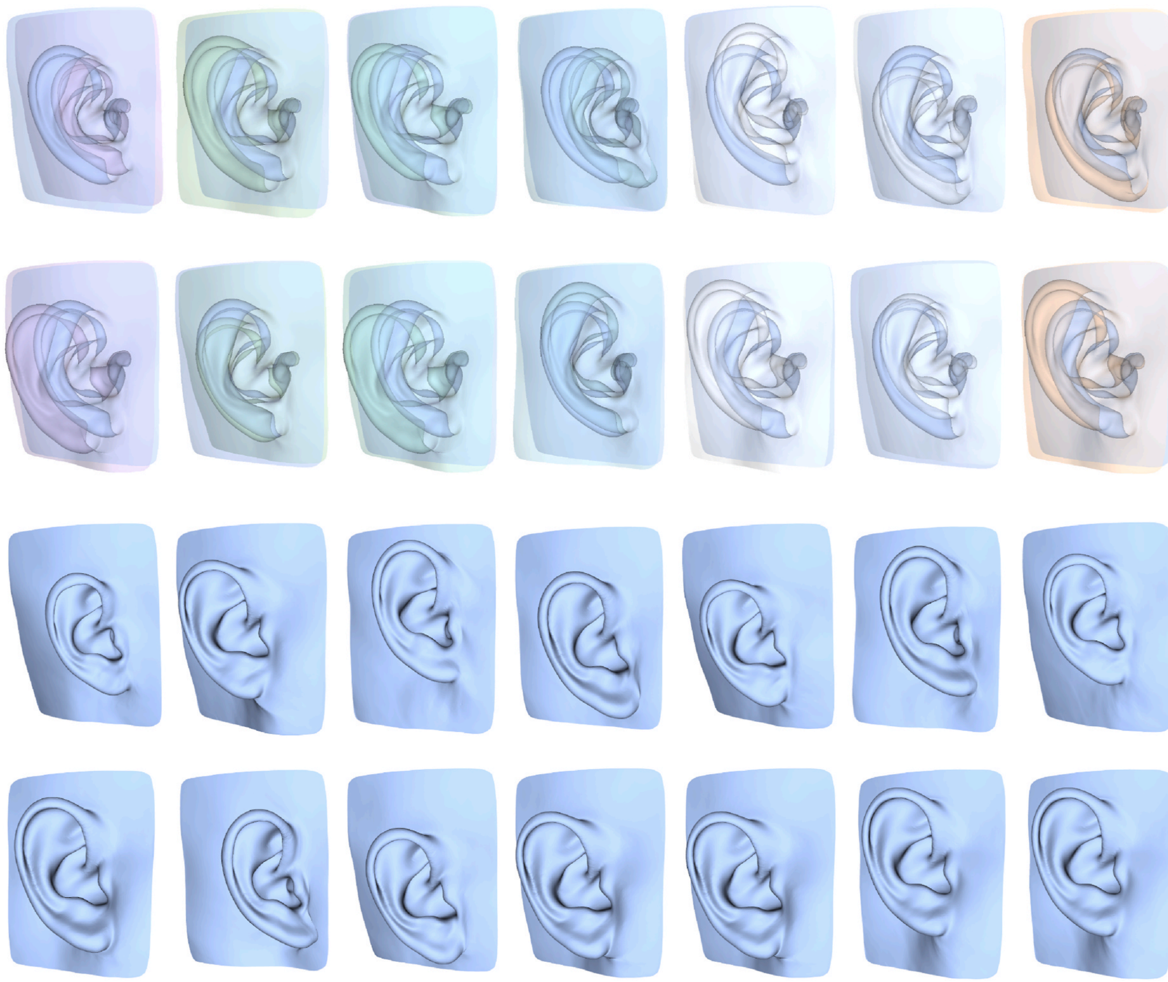

Fig. 15. Boundary ears on first 3 PCs overlaid with the mean ear (top) and individually (bottom).

4.3. Applications

The database and statistical model created in this study have broad applications to the design of devices that interact with the ear, including audio playback devices such as earbuds, hearing aids, and hearing protection.

Audio Devices – The comfort and performance of earbuds and similar devices that are intended to rest in the concha and ear canal are strongly influenced by the geometric fit. Many designs rely on the tragal notch to hold the device in place as the user moves. However, the current study demonstrates a large range of variability in tragal notch geometry that needs to be taken into account in design. The current study also demonstrates that the outer canal has an oval rather than round cross section. This information is not new to audiologists and others who work regularly with the ear, but it contrasts with the commonly round earbud design.

Hearing Aids – Many different design approaches to hearing aids are observed in the market. In addition to providing detailed information on concha and canal shape, the current model includes an accurate representation of the scalp adjacent to the ear. The area between the pinna and the scalp is often used to hold hearing aid components, and the current model provides a better representation of this area than any other available model. This is in part because this is accurately extracted from the CT data but is difficult to access with an optical scanner. Moreover, the current model is not affected by hair artifacts, which contaminate all other databases that include the scalp adjacent to the ear. The inclusion of the full ear canal may also be an advantage for modeling of the audio performance of the hearing aid, although as noted above the unknown precision in the estimate of the ear drum location may limit the utility for this purpose.

Hearing Protection – Both in-ear and over-ear hearing protection designs can benefit from the current data. The in-ear benefits are comparable to those for in-ear audio and may be similar to the utility of other databases, but the current database has unique benefits for over-ear protection (and for headphones), because the ear is located within a head-based coordinate system. This means that the positions and orientations of the ears relative to the head area that will support the devices, whether with a strap over the top of the head or behind the head. Quantifying the ears relative to the head also has substantial advantages when the hearing device also has a microphone intended to pick up the user's speech. For these applications, knowing the relative location of the mouth is useful.

4.4. Future work

Future studies will add more ears to the dataset. Although the current dataset is not small compared with what has been published before, ears very widely in the human population, with enough idiosyncrasy that they can be used as biometrics for identification. Hence, a larger dataset will be valuable.

In addition to adding subjects, extending and quantifying the population with respect to race and ethnicity will be valuable. Importantly, we may be able to quantify the extent to which the current dataset is representative of, for example, the U.S. population by access to exterior

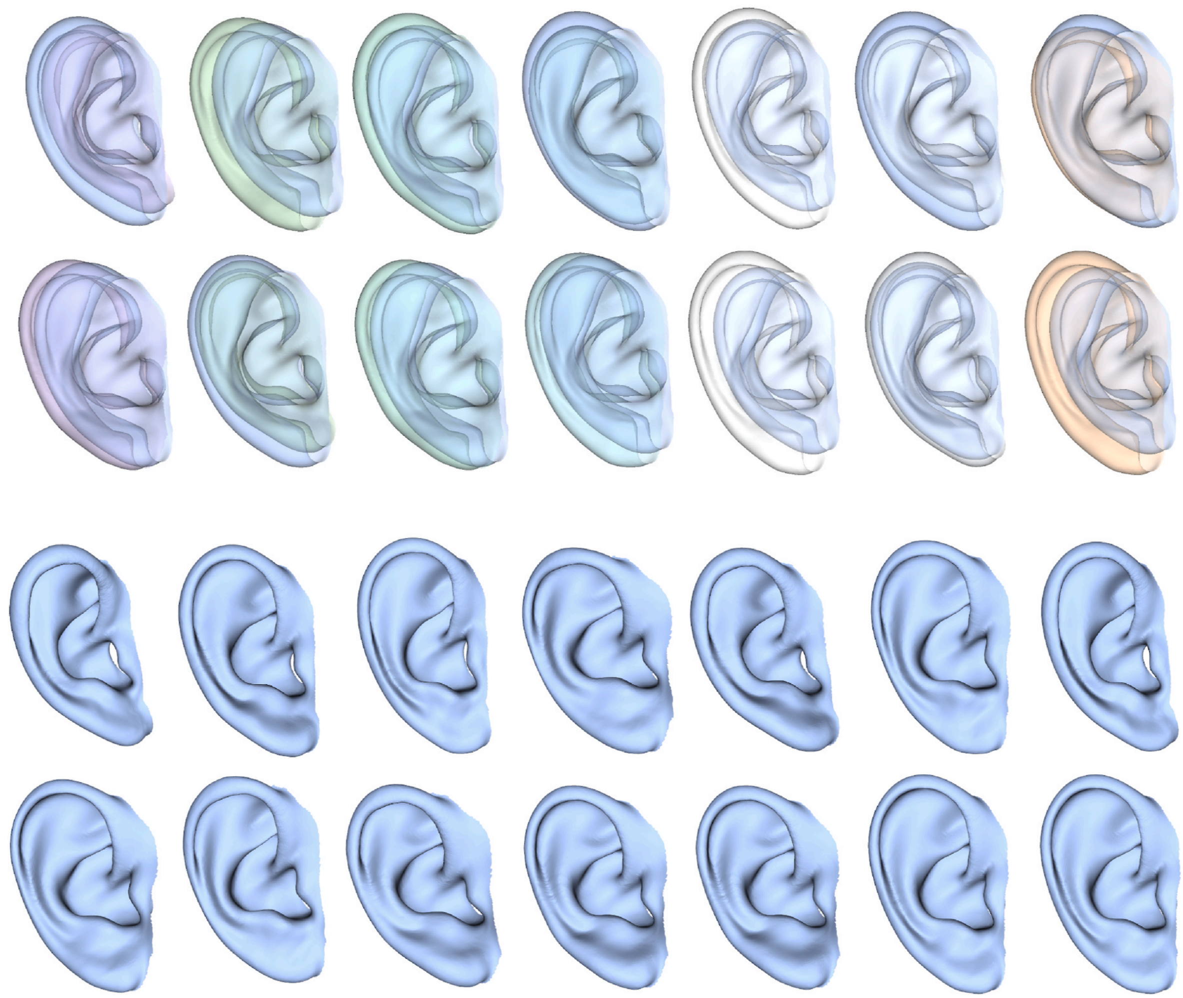

Fig. 16. Boundary ears on first 3 PCs for the pinna overlaid with the mean ear (top) and individually (bottom).

ear geometry only. That is, we can use the model to fit exterior ear shapes for scans of subjects who have reported race/ethnicity data. We can then impute those values for the current dataset. We note that race is a social construct, and we are only interested in it to the extent that it is correlated with size and shape differences. Similarly, we hope to collaborate with researchers who have access to surface scan data for ears in other national populations. Due to the expressiveness of the current PC model, fitting and comparing new data is much easier than the processes needed to build the original dataset.

Future work will also include integrating the ear model with a statistical head shape model (Park et al., 2021). Head integration will improve the utility of the dataset and model for a wide range of additional analyses, including the design of head-worn audio devices, such as over-the-ear headphones, and opens the possibility of computing head-related transfer functions (HRTF) to support spatial audio applications.

CRediT authorship contribution statement

Matthew P. Reed: Writing – review & editing, Writing – original draft, Validation, Supervision, Software, Resources, Project administration, Methodology, Investigation, Funding acquisition, Formal analysis, Conceptualization. **Tyler R. Vallier:** Writing – review & editing, Supervision, Software, Methodology, Investigation, Formal analysis, Data curation. **Anne C. Bonifas:** Writing – review & editing, Writing – original draft, Supervision, Software, Methodology, Investigation, Formal analysis, Data curation.

Ethical approval

This research was performed under the approval of an Institutional Review Board at the University of Michigan (HUM# HUM00004842).

Funding

This work was supported by Amazon, Inc.

Declaration of competing interest

The authors declare the following financial interests/personal relationships which may be considered as potential competing interests: Matt P. Reed reports financial support was provided by Amazon (Award #AWD020495). If there are other authors, they declare that they have no known competing financial interests or personal relationships that could have appeared to influence the work reported in this paper.

Acknowledgments

We thank our collaborators at Amazon, including Mihir Shetye and Alex Epstein. At UMTRI, several students contributed to the data extraction and processing, including Alec Murrell, Samarth Kadambi, and Wuyuqing Yang.

Data availability

The data that has been used is confidential.

References

Alexander, K.S., Stott, D.J., Sivakumar, N.K., 2011. A morphometric study of the human ear. J. Plast. Reconstr. Aesthetic Surg. 64, 41–47.

Baloch, S., Zouhar, A., Fang, T., 2011. Deformable registration of organic shapes via surface intrinsic integrals: application to outer ear surfaces. In: Menze, B., Langs, G., Tu, Z., Criminisi, A. (Eds.), Medical Computer Vision. Recognition Techniques and Applications in Medical Imaging, Lecture Notes in Computer Science, vol. 6533. Springer, Berlin, Heidelberg. https://doi.org/10.1007/978-3-642-18421-5_2. MCV 2010.

Balouch, K.B., Durkee, H.E., Farrar, R.M., Sok, M., Keefe, D.H., Remenschneider, A.K., Horton, H.J., Voss, S.E., 2023. Measurements of ear-canal geometry from high-resolution CT scans of human adult ears. Hear. Res. 434.

Cintas, C., Quinto-Sánchez, M., Acuña, V., et al., 2017. Automatic ear detection and feature extraction using Geometric Morphometrics and convolutional neural networks. IET Biom. 6 (3), 221–233.

Chu, Y., Zhang, K., Wei, H., Wang, Y., 2019. Template-based ear modeling and reconstruction. Proc. 2019 Chinese Automation Congress.

Fantini, D., Avanzini, F., Ntalampiras, S., Presti, G., 2021. HRTF individualization based on anthropometric measurements extracted from 3D head meshes. Immersive and 3D (I3DA). https://doi.org/10.1109/I3DA48870.2021.961090.

Farkas, L.G., 1978. Anthropometry of normal and anomalous ears. Clin. Plast. Surg. 5 (3), 401–412.

Fernanda, A., Gentil, F., Tavares, J., 2014. Segmentation algorithms for ear image data towards biomechanical studies. Comput. Methods Biomech. Biomed. Eng. 17 (8), 888–904. https://doi.org/10.1080/10255842.2012.723700.

Fan, H., Yu, S., Wang, M., Li, M., Chu, J., Yan, Y., Harris-Adamson, C., 2021a. Analysis of the external acoustic meatus for ergonomic design: part I–measurement of the external acoustic meatus using casting, scanning and rapid estimation approaches. Ergonomics 64 (5), 640–656.

Fan, H., Yu, S., Wang, M., Li, M., Zhao, X., Ren, Y., Harris Adamson, C., 2021b. Analysis of the external acoustic meatus for ergonomic design: part II–anthropometric variations of the external acoustic meatus by sex, age and side in Chinese population. Ergonomics 64 (5), 657–670.

Fryar, C.D., Carroll, M.D., Gu, Q., Afful, J., Ogden, C.L., 2021. Anthropometric reference data for children and adults: United States, 2015–2018. National Center for Health Statistics. Vital Health Stat 3 (46).

Fu, F., Luximon, Y., 2020. A systematic review on ear anthropometry and its industrial design applications. Human Factors Manufact. 30, 176–194.

Ji, X., Zhu, Z., Gao, Z., Bai, X., Hu, G., 2018. Anthropometry and classification of auricular concha for the ergonomic design of earphones. Human Factors Manufact. 28, 90–99.

Kamboj, A., Rani, R., Nigam, A., 2020. A comprehensive survey and deep learning-based approach for human recognition using ear biometric. Vis. Comput. 38, 2383–2416.

Lee, W., Yang, X., Jung, H., Bok, I., Kim, C., Kwon, O., Heecheon, Y., 2018. Anthropometric analysis of 3D ear scans of Koreans and Caucasians for ear product design. Ergonomics 61 (11), 1480–1495. https://doi.org/10.1080/00140139.2018.1493150.

Liu, B.-S., 2008. Incorporating anthropometry into design of ear-related products. Appl. Ergon. 39, 115–121, 2008.

Lu, P., Tsao, L., Yu, C., Ma, L., 2021. Survey of ear anthropometry for young college students in China and its implications for ear-related product design. In: Human Factors in Manufacturing, vol. 31. PyMeshLab. Zenodo, pp. 86–97. https://doi.org/10.5281/zenodo.4438750. Muntoni, A., and Cignoni, P. (2021.

Musy, M., et al., 2023. *vedo*, a python module for scientific analysis and visualization of 3D objects and point clouds. Zenodo. https://doi.org/10.5281/zenodo.7019968.

Niemitz, C., Nibbrig, M., Zacher, V., 2007. Human ears grow throughout the entire lifetime according to complicated and sexually dimorphic patterns — conclusions from a cross-sectional analysis. Anthropol. Anzeiger 65 (4), 391–413.

Park, B.-K., Corner, B.D., Hudson, J.A., Whitestone, J., Mullenger, C.R., Reed, M.P., 2021. A three-dimensional parametric adult head model with representation of scalp shape variability under hair. Appl. Ergon. 90, 103239.

Paulsen, R., Larsen, R., Nielsen, C., Laugesen, S., Ersboll, B., 2002. Building and testing a statistical shape model of the human ear canal. In: Doh, Kikinis (Ed.), Of *Medical Image Computing And Computer Assisted Interventions* 2002. Springer, Berlin, pp. 373–380.

Peterson, W.W., et al., SciPy 1.0 Contributors, 2020. SciPy 1.0: fundamental algorithms for scientific computing in Python. Nat. Methods 17 (3), 261–272.

Pollack, K., Majdak, P., Furtades, H., 2020. A parametric pinna model for the calculations of head-related transfer functions. Forum Acusticum, Lyon, France 1357–1360. https://doi.org/10.48465/fa.2020.0280.hal-03235345.

Schroeder, W., Martin, K., Lorensen, B., 2006. The Visualization Toolkit, fourth ed. Kitware. 978-1-930934-19-1.

Sforza, C., Grandi, G., Binelli, M., Tommasi, D.G., Rosati, R., Ferrario, V.F., 2009. Age- and sex-related changes in the normal human ear. Forensic Sci. Int. 187, 110e1–110e7.